Geophysical Journal International

Geophys. J. Int. (2015) **200,** 627–637
GJI Seismology

doi: 10.1093/gji/ggu421

Monsoon-induced earthquake activity in Talala, Gujarat, India

S. Hainzl,[1] S. K. Aggarwal,[2] P. K. Khan[3] and B. K. Rastogi[2]

[1] *GFZ German Research Centre for Geosciences, Potsdam, Germany. E-mail: hainzl@gfz-potsdam.de*
[2] *Institute of Seismological Research, Raisan, India*
[3] *Indian School of Mines, Dhanbad, India*

Accepted 2014 October 27. Received 2014 October 27; in original form 2014 July 4

SUMMARY

We explore the possibility that the episodic swarm activity observed in the region around Talala is related to a poroelastic response of the seismogenic crust to surface water flux, leading to pore pressure changes at depth. In particular, we evaluate models where these pore-pressure changes result from rainfall-induced ground-water recharge with corresponding pore pressure diffusion into depth and reservoir-induced pressure changes related to two dams located around 10 km from the swarm region. Based on the observed reservoir and rainfall data, we estimate the time-dependent pressure variations in the active seismogenic volume and calculate the resulting seismicity rates assuming rate- and state-dependent frictional nucleation. Our results show that pore pressure variations can well explain the general observations, with highest correlations for the reservoir-triggering mechanism. However, the latter model requires unrealistically small values of effective normal stresses in the source region unless pore-pressure diffusion is guided by a highly permeable fracture zone.

Key words: Earthquake dynamics; Seismicity and tectonics; Statistical seismology.

1 INTRODUCTION

Crustal seismicity has been partly explained by hydromechanical coupling where increased pore fluid pressure reduces the effective normal stress and thus the strength of faults, promoting earthquake failures (Costain & Bollinger 2010). Triggering of earthquakes is evident for fluid injections in wells, for example (Zoback & Harjes 1997; Shapiro *et al.* 2003; Fischer *et al.* 2008), where engineering data are available and dense monitoring systems are installed. Furthermore, it is known that the filling as well as seasonal variations of reservoirs can trigger local earthquakes, for example (Talwani 1997; Gahalaut & Hassoup 2012). A less-known source of hydroseismicity is rainfall, which leads to pore-pressure changes in the crust due to the infiltration of water in the ground. While previous evidence came mainly from positive statistical correlations between rainfall and seismicity (Muco 1995; Svejdar *et al.* 2011), Hainzl *et al.* (2006, 2013b) performed a quantitative physical analysis of this triggering process for the case study of the seismicity occurring below Mt Hochstaufen, SW Germany. Based on Coulomb stress calculations and the assumption of rate- and state-dependent frictional nucleation they could show that rainfall seems to be the dominant triggering process in this specific location. However, this case might be an exception because it is a Karst region where the effect of rainfall might be amplified by accumulation of water in open fracture systems (Miller 2008). To clarify this point, similar analysis has to be performed for other case studies.

Here we focus on the swarm activity observed in the Talala, Gujarat, region in India, where swarms have been recorded in the past years which seem to occur with some delay after the monsoon. In addition, two reservoirs are located only about 10–20 km from the active region. To explore whether or not the reservoirs, or rainfall, or both can explain the observed seismicity, we perform a comprehensive analysis based on stress calculations and laboratory-derived friction laws. While this modelling approach has already been previously applied to aftershock sequences (Catalli *et al.* 2008; Hainzl *et al.* 2009) and rainfall-triggered seismicity (Hainzl *et al.* 2006, 2013b), it is to our knowledge the first time that such a quantitative seismicity model is used in the context of reservoir-triggered seismicity. In particular, it offers the possibility to account for simultaneous sources in a physically meaningful way, such as the combination of pore-pressure changes due to an areal penetration of water into the ground and the localized load and infiltration at reservoirs.

2 GEOLOGY AND SEISMICITY DATA

The Talala region is located in Junagadh district of south Saurashtra peninsula uplifted horst province of Gujarat, western India (Fig. 1). The surface geology is occupied by Deccan Trap basalt forming the plateaus and conical ridges in major parts of Saurashtra peninsula including Talala area. The coastal plains fringing the Trappean highland comprises Cenozoic cover consisting of Tertiary and Quaternary sediments (Biswas 1987). The three active faults are identified in Talala area named as Girnar Fault (NE–SW trending), F1 (E–W trending) and F2 (WNW–ESE trending; Gandhi *et al.* 2014). The geomorphic indices indicate the active tectonics along

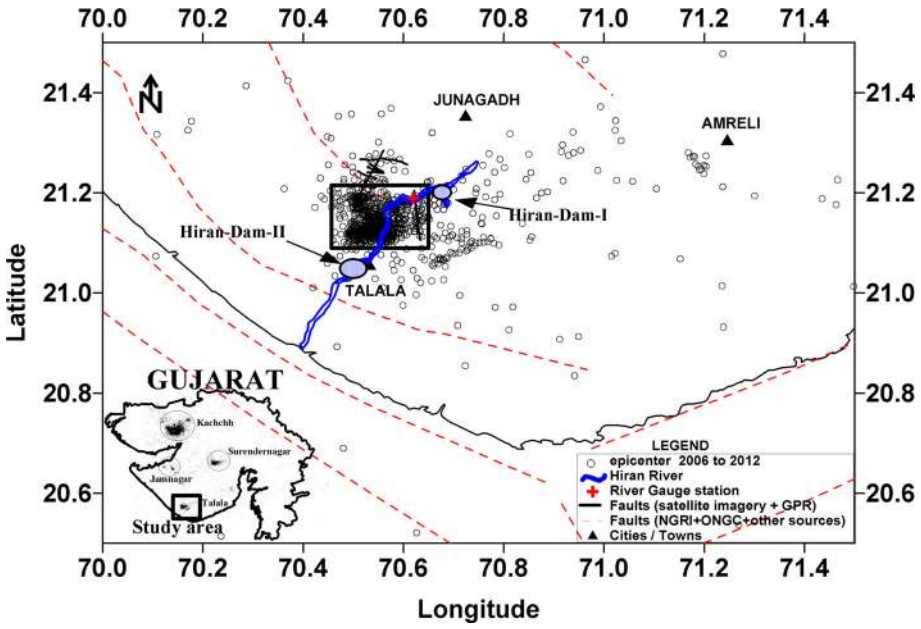

Figure 1. Map of the analysed region with observed seismicity, fault traces, and the locations of the two reservoirs as well as the river gauge station analysed in this study. The small inset on the lower left-hand corner shows the broader region with its localized seismicity clusters.

longitudinal river profiles (Hiran, Devka, Megal and Noli rivers) and in the past decade the region has experienced four significant seismicity swarms during 2001, 2004, 2007 and 2011 soon after the monsoon and lasted for 2–3 months (Rastogi *et al.* 2012). The swarm of year 2007 and 2011 was monitored by Gujarat Seismic Network (GSNet) operated by Institute of Seismological Research, Gandhinagar, Gujarat. During these swarms the region has reported several thousand of felt shocks, thousands of shocks are reported in seismic network and hundreds of events are located with magnitude range 1.0 to 5.1 M_w (Rastogi *et al.* 2012) as shown in Fig. 1. A catalogue of about 1000 events has been prepared with a minimum magnitude of 1.0, for the Talala region and some 700 earthquakes with magnitude larger than the completeness magnitude $M_c = 1.75$ (Fig. 2). In the following, we analyse the $M \geq 1.7$ earthquakes in this catalogue spanning the 6 yr from 2007 January 1 to 2012 December 31.

2.1 Statistical test for transient forcing

Before examining the potential mechanism of surface water induced seismicity, we check that the seismicity cannot be simply explained by constant tectonic forcing and earthquake-induced stress changes. For this purpose, we apply the recent approach of Marsan *et al.* (2013), which has been further tested and applied by Hainzl *et al.* (2013a). The method attempts to statistically separate background $r(t)$ and aftershock $\nu(t)$ rates, where the latter is related to earthquake–earthquake interactions. The observed earthquake rate $\lambda(t)$ is assumed to be the sum of both terms, $\lambda(t) = r(t) + \nu(t)$. The interaction term $\nu(t)$ accounts for the well-known empirical relations regarding the temporal power-law decay of triggered aftershock activity and the exponential dependence of the aftershock productivity on the main shock magnitude. In particular, it is modelled using the epidemic type aftershock sequence (ETAS) model (Ogata 1988)

$$\nu(t) = \sum_{i:t_i<t} K e^{\alpha(M_i - M_c)} (c + t - t_i)^{-p} \quad , \tag{1}$$

where t_i and $M_i \geq M_c$ are the occurrence times and magnitudes of the observed earthquakes. The parameters c and p are related to the Omori-Utsu aftershock decay law (Utsu *et al.* 1995), while K and α describe the magnitude-dependent aftershock productivity. All parameters are estimated by the maximum likelihood method, yielding the optimal parameters $c = 0.008$ d (12 min), $p = 1.34$, $K = 0.0082$ and $\alpha = 1.2$. These values are generally in the range of values observed at tectonic plate boundaries, but the relative low α-value is indicative for swarm-type activity (Enescu *et al.* 2009; Hainzl *et al.* 2013a). Based on the Akaike Information Criterion (AIC), we find that the background forcing term $r(t)$ is significantly time-dependent and accounts for 62 per cent of the activity; that is, 38 per cent of the earthquakes are identified as aftershocks. The estimated activity which cannot be associated to earthquake–earthquake interactions (background forcing term) is shown in Fig. 2(b), clearly indicating transient (time-dependent) behaviour.

3 CORRELATIONS WITH HYDROLOGICAL OBSERVATIONS

Earthquake activity observed in Talala region mostly starts soon after monsoon with a delay of a few weeks and then continues for a 2–4 months period. The monsoon supplies the river Hiran with water, which is passing through the seismicity region Talala and is impounded at the two dams Hiran I and II (see Fig. 1), established mainly for agriculture and domestic purpose. The river flows only during monsoon season and both reservoirs are only fully flooded during a few weeks to months in the year. Hiran I and II are earthen dams on basalt rock terrain with catchment areas of 81 and 341 km^2, respectively. The Hiran I was commissioned in year 1959 and Hiran II was commissioned in year 1973, where data are available since year 1983. The rainfall data is available for this period and it is reported that heavy rainfall occurs during year 2007 and 2011. Due to heavy rain Hiran II flooded with 1036 cusecs and Hiran I with 60 cusecs maximum inflow. A river gauge station located at latitude 21.18N and longitude 70.63E on Hiran river was established since

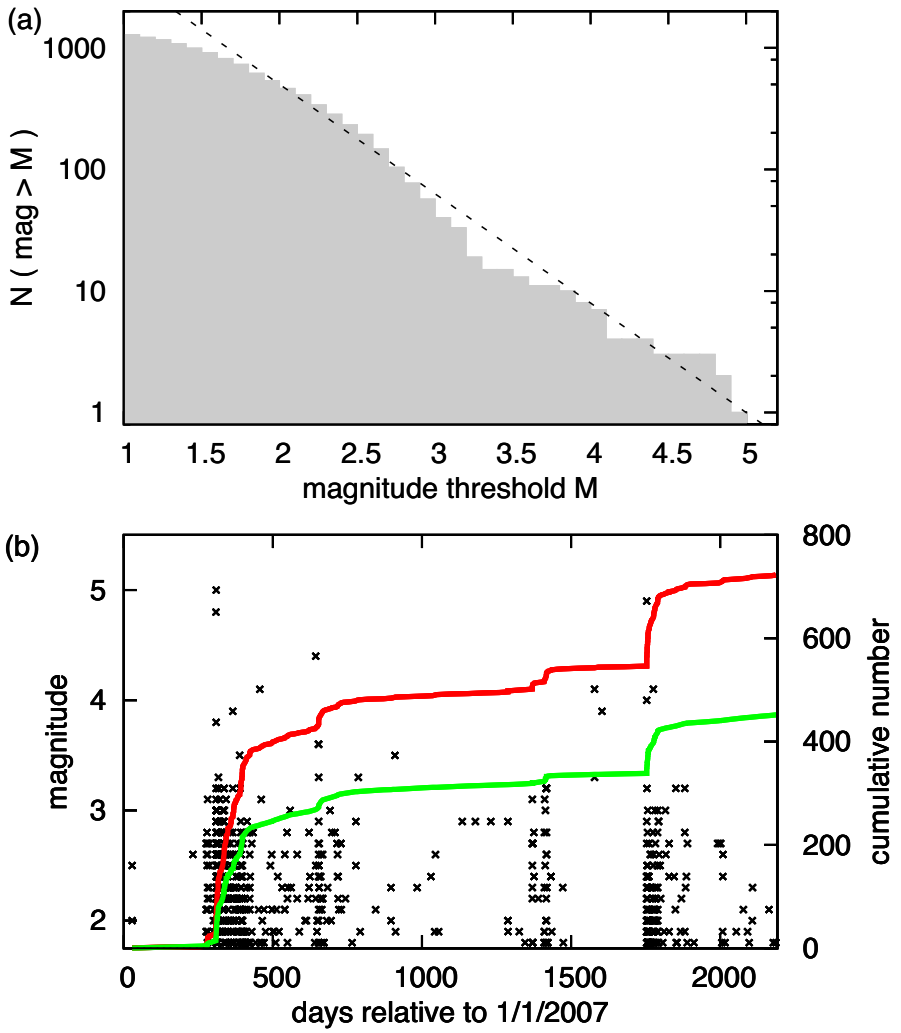

Figure 2. (a) Frequency–magnitude distribution of the earthquakes. The dashed line refers to a *b*-value of 0.9. (b) The magnitude versus time plot of $M \geq 1.75$ events. Additionally, the curves (with labels on the right) show the corresponding cumulative number of events (red line) and the fraction related to background activity (green line).

1990 recording flow rates which can be in general used as proxy for groundwater level changes (Costain & Bollinger 2010).

We use these observed hydraulic parameters, which are presented in Fig. 3, to analyse the triggering mechanism of the earthquake activity in Talala, Gujarat region. In a first analysis, we determine the cross-correlations between these hydraulic observables and the observed seismicity. For this analysis, we transform the point-occurrences of the earthquakes into a continuous earthquake rate function by smoothing the observed occurrences. Because the correlation might depend on the smoothing window, we calculated the result for two different cases: (i) binned activity in a moving window of 1 d and (ii) activity smoothed by a normal distribution with standard deviation of 30 d. The results are shown in Fig. 4. Significant positive correlations are observed for all data sets, where the maximum correlation occurs for a causal, positive delay of the seismicity. The delay of the seismicity is particularly clear for the rainfall and runoff data for which a positive correlation is only observed for delays larger than approximately 25 d with a maximum between 80 and 100 d. With smaller delays and even higher values is the seismicity found to be correlated with the reservoir levels, where a broad region with positive correlation coefficients is observed between −100 and 100 d with a maximum around 25 d.

In the case of the rainfall-triggering mechanism, the variation of the groundwater level is the decisive quantity affecting pore-pressure changes in depth. Thus we have estimated the variations of the groundwater level based on the observed rainfall data and simple model assumptions, because direct measurements of the groundwater level are missed. For this purpose, we assumed that the temporal change of the water table $\mathrm{d}W/\mathrm{d}t$ is equal to the difference between recharge rate Q and the ground water discharge rate DR. The latter depends on the unknown depth of the water head z according to $DR = DR_{\max} \exp(-\eta z)$ (Niu *et al.* 2007), where we set the parameters to $\eta = 1.25\ \mathrm{m}^{-1}$ and $DR_{\max} = 4.5 \times 10^{-3}\ \mathrm{mm\ s}^{-1}$. However we found that our results are not crucially depending on the specific choice of these parameters. For the recharge rate, we used two end-member models: (i) simultaneous recharge with rainfall (T0d) and (ii) a diffusion-type penetration of the rain water through a soil layer with low hydraulic diffusivity (T50d). The latter model leads to a maximum of the response function at a delay time of $w^2/(2D_0)$ for a layer of width w and hydraulic diffusivity D_0. The instantaneous recharge model leads to groundwater changes with higher correlations than all direct measurements, but the maximum correlation still occurs with a delay of 50 d (Fig. 4). Thus we choose for case (ii) a delay time of the peak response function of 50 d by setting the parameters

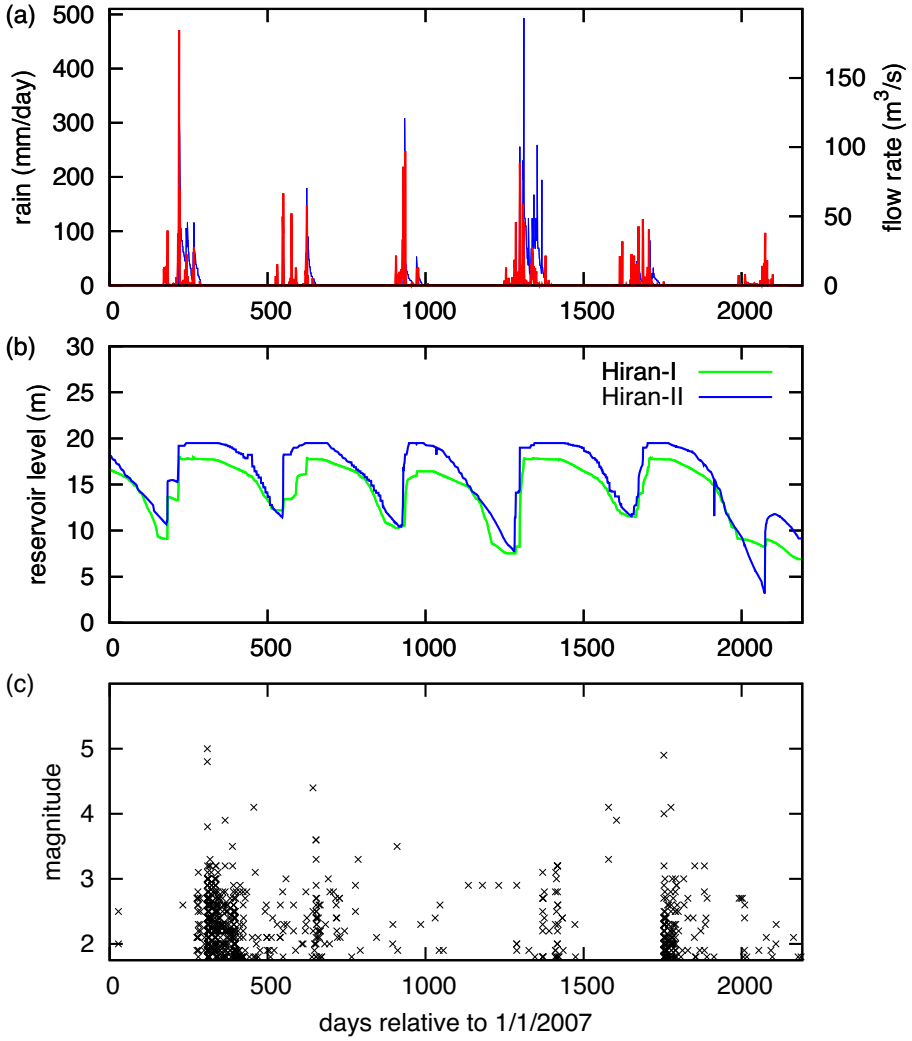

Figure 3. Temporal dependence of the observables in Talala, Gujarat, region: (a) rainfall (red) and river flow rates (blue), (b) reservoir water levels and (c) occurrences of $M \geq 1.75$ earthquakes.

$w = 2$ m and $D_0 = 5 \times 10^{-7}$ m^2 s^{-1} which is a reasonable value for soil (Evangelides *et al.* 2010). Consequently, the corresponding groundwater level changes are in this case almost synchronous with the seismicity rates but with slightly smaller correlation values.

Usually river flow (runoff) data can be alternatively used to estimate the groundwater changes (Costain & Bollinger 2010). However, the Hiran river is not perennial and only flows in monsoon periods, when the stream is stored in dam Hiran I and II. During the rest of the year, the groundwater level is below the river level and cannot be approximated by flow rates. For this reason, we could not use the available flow data for our modelling of crustal stress changes and earthquake rates as presented in the following sections.

The high correlations of the observed seismicity with the reservoir filling motivates us to perform in the next sections a detailed comparison of the observations with seismicity rates expected from rate- and state-dependent frictional nucleation of earthquakes in response to the reservoir-induced stress changes. However, because the seasonal variations of the reservoir levels can be roughly approximated by boxcar functions, we can first perform a qualitative comparison based on analytic expressions for the migration of the pore-pressure front and back front in the case of pore-pressure diffusion. In a homogeneous isotropic medium, a sudden pressure increase of a point source (at time $t = 0$) initiates a propagating pore-pressure front which defines the onset of the pressure increase at distance r from the pressure source according to

$$r = \sqrt{4\pi Dt}\,, \tag{2}$$

where D is the hydraulic diffusivity (Shapiro *et al.* 1997). The sudden stress drop at the end of the boxcar function (at time t_0) leads to a similar propagation front describing the onset of stress drop for $t > t_0$, the so-called back front, which can be described by Parotidis *et al.* (2004)

$$r = \sqrt{2nDt\left(\frac{t}{t_0} - 1\right)\ln\left(\frac{t}{t - t_0}\right)}\,, \tag{3}$$

with $n = 1$, 2 or 3 for pore-pressure diffusion in 1, 2 or 3 dimensions, respectively. At any location, earthquakes are generally expected to occur in the time period of increasing pore pressures, when Coulomb failure stresses are increasing due to decreasing effective normal stress. Thus the time period between front and back front is expected to enclose the majority of earthquakes. We tested this assumption by plotting these time periods as a function of the distances to the reservoirs Hiran I and II in Fig. 5. We find that for a hydraulic

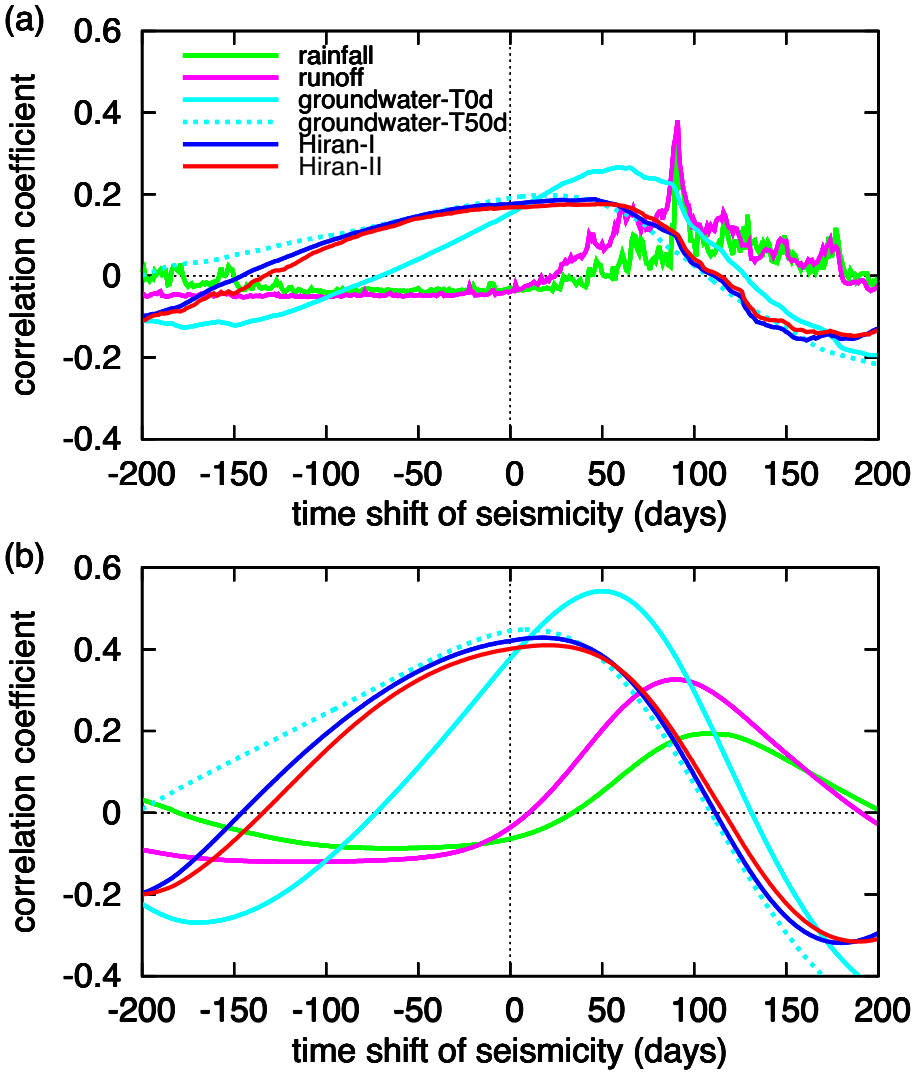

Figure 4. Cross-correlation coefficients between surface water observations (reservoir levels, rainfall and runoff data) and seismicity, where correlation coefficients are calculated for (a) daily binned earthquake numbers and (b) Gaussian-smoothed numbers with standard deviation of 30 d. Additionally, the correlations are shown for the modelled groundwater level based on the surface rainfall in the case of immediate recharge (T0d) and delayed recharge due to diffusion-type penetration through a surface layer leading to a peak delay of the groundwater recharge of 50 d (T50d).

diffusivity $D = 5$ m^2 s^{-1}, which is in the order of previously estimated values for fracture systems (Costain & Bollinger 2010), almost all earthquakes in the study region occurred inside these periods indicating that reservoir-induced stress variations might be one triggering mechanism for the observed earthquakes. Thus we analyse in more detail both reservoir and rainfall triggering in the following sections.

4 SEISMICITY MODEL

We apply the well-known earthquake generation model introduced by Dieterich (1994) which accounts for Coulomb-stress changes and rate- and state-dependent frictional nucleation observed in experimental data. The main assumptions of this model are that a large number of potential nucleation sites exist in any volume and that earthquakes are nucleating independently of each other. In this model approach, the earthquake nucleation rate R depends on the state variable γ, the constant tectonic background stressing rate $\dot{S}$ and the background seismicity rate r according to

$$R = \frac{r}{\gamma \dot{S}}\,. \tag{4}$$

The evolution of the state variable is governed by

$$\mathrm{d}\gamma = \frac{1}{A\sigma}\left[\mathrm{d}t - \gamma \mathrm{d}S\right], \tag{5}$$

where S is the Coulomb failure stress, σ is the effective normal stress and A is a dimensionless fault constitutive friction parameter usually estimated as ~0.01 (Dieterich 1994; Dieterich *et al.* 2000).

The Coulomb failure stress is calculated by

$$S = \tau + \mu_{\mathrm{eff}}(\sigma_{\mathrm{n}} + p), \tag{6}$$

with effective friction coefficient $\mu_{\mathrm{eff}} = (\mu - \alpha')$, where α' is a dimensionless constant having typical laboratory values in the range 0.25–0.5. In (6), τ is the shear stress in the direction of slip on the assumed causative fault plane, σ_{n} is the normal stress changes (positive for unclamping or extension) and p is the pore pressure (King & Cocco 2001). The total pore pressure is the result

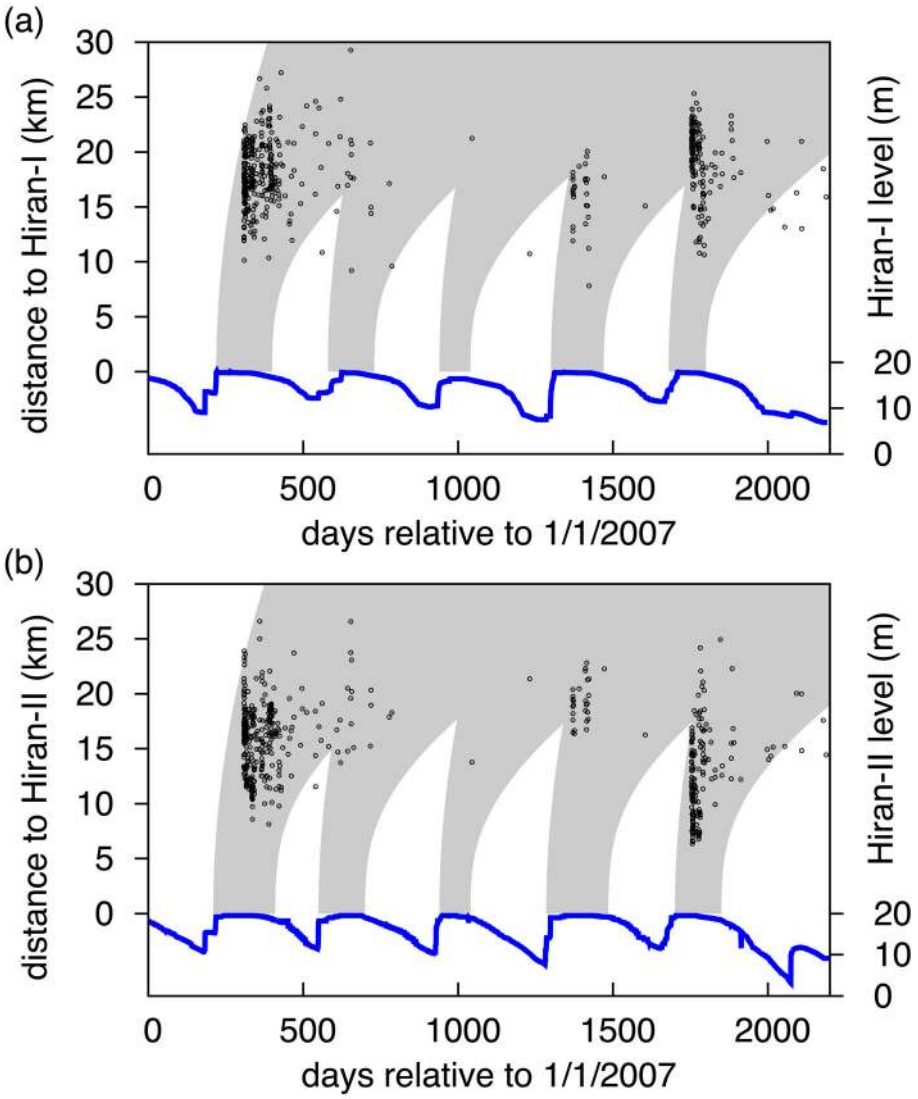

Figure 5. Distances of earthquakes to the reservoirs (a) Hiran I and (b) Hiran II as a function of time. The points refer to $M \geq 1.75$ earthquakes occurred between longitude 70.45° and 70.6°, and latitude 21.08° and 21.2°. The locations are compared with analytic solutions for pore pressure diffusion eqs (2) and (3) with $D = 5$ m^2 s^{-1} and $n = 1$ (grey shaded). In both plots, the curve refers to the corresponding reservoir level (with scale on the right-hand side).

of possible pore pressure diffusion p_d and instant compression p_c which depends on the volumetric stress. It is given by

$$p = p_d + p_c = p_d - B(\sigma_{11} + \sigma_{22} + \sigma_{33})/3, \quad (7)$$

where B is the Skempton coefficient which varies between 0 and 1 and σ_{ij} defines the stress tensor (Cocco & Rice 2002).

For an arbitrary stressing history consisting of a transient stress changes $\triangle S(t)$ in addition to the constant tectonic loading rate $\dot{S}$, the evolution of γ can be tracked by considering sufficiently small time steps leading to stress increments of $\Delta S(t)$ during time intervals of Δt. Implementing the stress-step in the centre of the time step Δt, the state variable is iterated according to

$$\gamma(t + \Delta t) = \left(\gamma(t) + \frac{\Delta t}{2A\sigma}\right) \exp\left(-\frac{\dot{S}\Delta t + \triangle S(t)}{A\sigma}\right) + \frac{\Delta t}{2A\sigma} \quad (8)$$

starting from the background level, that is, $\gamma(0) = 1/\dot{S}$ (Hainzl *et al.* 2010).

Tectonic forces alone would lead to a continuous stress change with constant stressing rate and thus to a constant background seismicity rate. However, our test in Section 2.1 shows that the background rate is strongly time-dependent in the Talala region, indicating that the stressing rate is not constant. In the following, we explore the potential impact of surface water induced stress changes on the recorded seismicity.

4.1 Rainfall-induced stress changes

We assume that the groundwater table is coupled with an underlying fluid-saturated poroelastic rock. Based on the estimated changes of the groundwater level, we calculate the pore pressure changes at seismogenic depth assuming a 1-D model. We focus on the direct effects of pore pressure variations and ignore effects such as strain-dependent hydraulic diffusivity. In this case, the pore-pressure change at depth z in response to a step change of the groundwater level $\triangle W$ at time $t = 0$ can be calculated by Roeloffs (1988) and Simpson (2001)

$$\triangle p(z, t) = \left[(1 - \alpha)\,\mathrm{erfc}\left(z/\sqrt{4Dt}\right) + \alpha\right] \rho g \triangle W, \quad (9)$$

with gravitational acceleration g and water density ρ. The parameter α is related to the Skempton coefficient B and the Poisson ratio ν as $\alpha = B(1 + \nu)/[3(1 - \nu)]$. In the subsequent analysis, we assume the standard values $\nu = 0.3$ and $B = 0.5$. By convolution of the groundwater level changes with this response function, we get the pore pressure changes $\triangle p(z, t)$ at depth in response to the measured surface rain. The related time-series of Coulomb failure stress changes at depth z is given by $\triangle S_{RA}(z, t) = \mu_{\rm eff}\triangle p(z, t)$ according to eq. (6).

4.2 Reservoir-induced stress changes

To calculate the reservoir-related stress variations, we follow the calculations of Gahalaut & Hassoup (2012) assuming an uniform and isotropic half-space. The total pressure change $\triangle p$ related to a reservoir is the sum of $\triangle p_c$ and $\triangle p_d$, which are the change in pore pressure due to the instant compression caused by the reservoir load, and the change in pore pressure due to the diffusion of reservoir water load, respectively (Roeloffs 1988). The instant effect $\triangle p_c$ can be calculated by the last term of eq. (7), where stress changes σ_{ii} are calculated using 3-D Boussinesq–Cerruti solutions for a point force acting on the surface of an infinite half-space (see e.g. Deng *et al.* 2010). For that purpose, we represented the Hiran I and II reservoirs by 9, respectively 16 point sources covering the reservoir surface. The pressure change related to diffusion is calculated by the convolution of the observed reservoir water level L with the Green's function G:

$$\triangle p_d(x, y, z, t) = D \int_0^t \int_{-\infty}^{\infty} \int_{-\infty}^{\infty} L(\bar{x}, \bar{y}, \bar{t})\, G(x - \bar{x}, y - \bar{y}, z, t - \bar{t})\, \mathrm{d}\bar{t}\, \mathrm{d}\bar{x}\, \mathrm{d}\bar{y}$$

$$\text{with } G(x - \bar{x}, y - \bar{y}, z, t - \bar{t}) = \frac{z}{8\pi^{1.5}[D(t - \bar{t})]^{2.5}} \exp\left(-\frac{(x - \bar{x})^2 + (y - \bar{y})^2 + z^2}{4D(t - \bar{t})}\right), \quad (10)$$

where x, y and $\bar{x}, \bar{y}$ refer to horizontal coordinates of the observation and source points, respectively, and z is the depth of the observation. The related time-series of Coulomb failure stress changes at location x, y, z is given by $\triangle S_{R3D}(x, y, z, t) = \mu_{\rm eff}[\triangle p_c(x, y, z, t) + \triangle p_d(x, y, z, t)]$.

The above calculations assume homogeneous properties in the crust leading to 3-D diffusion of the pore pressure. However, if fracture zones with preferred orientations exist, the diffusion will become anisotropic. We evaluate the extreme case in which a high permeability channel is connecting the reservoirs and the active fault system. For that purpose, we use eq. (10) together with the Green's function for 1-D pore pressure diffusion (eq. 4 in Costain & Bollinger 2010). This model leads to the time-dependent stress change $\triangle S_{R1D}(x, y, z, t)$.

4.3 Computation procedure

Table 1 summarizes the model parameters that are used for calculating the stress changes related to the mechanisms described above. Because no specific values are known for the given region, the parameters are set to some typical values for rock (Mavko *et al.* 2009). However, we found that our results are not crucially depending on the specific choice. Based on these parameters, we calculated the stress change history at each node of a 3-D spatial grid which encloses the main earthquake activity. In particular, the stressing

Table 1. Description of model parameters.

Symbol	Description	Value
B	Skempton coefficient	0.5
ν	Poisson ratio	0.3
G	Shear modulus	30 GPa
$\mu_{\rm eff}$	Effective friction coefficient	0.4
D	Hydraulic diffusivity	0.1, 1.0, 5, 10, 50, 100 $\mathrm{m^2\ s^{-1}}$
$A\sigma$	Frictional resistance	Continuous values
$\dot{S}$	Tectonic stressing rate	Continuous values
r	Constant background rate	Continuous values

histories are calculated at a spatial grid between 70.45°–70.60° longitude and 21.08°–21.20° latitude (see box in Fig. 1) with step size of 0.01°. We scanned the depth range between 0 and 10.0 km, where most of the earthquakes are located, with step size of 1 km. For each grid node (x_j, y_j, z_j), we calculated the stressing history, that is the time-series of transients stress changes $\triangle S(x_j, y_j, z_j, t)$. To analyse the impact of the different mechanisms, we consider different combinations of the transient processes which are assumed to occur in addition to tectonic loading. For example, if both rainfall and reservoir mechanisms are considered simultaneously, the stress history is $\triangle S(x_j, y_j, z_j, t) = \triangle S_{RA}(z_j, t) + \triangle S_{R1/3D}(x_j, y_j, z_j, t)$. Based on a given stress history $\triangle S(x_j, y_j, z_j, t)$, the seismicity rate $R(x_j, y_j, z_j, t)$ is calculated by eqs (4) and (8) for each grid node. In the case of high-precision locations, we could directly compare the model forecasts with the observed seismicity at each location (x_i, y_i, z_i). However, due to the relative large location uncertainties and strong spatial clustering of our data set, we analyse the integrated rates over the seismogenic volume in order to get robust results. Thus the overall earthquake rate is calculated by summing the seismicity rate over all grid nodes in the seismogenic zone. Here we assume that the background rate is uniform.

The calculation depends on the model parameters r, $A\sigma$ and $\dot{S}$. These parameters are not well-constrained by independent observations. In particular, the effective normal stress σ and the tectonic stressing rate $\dot{S}$ can largely vary. The tectonic background seismicity rate r could be in principle estimated by declustering the seismicity observed in the past. However, because of missing local high-quality records in the past and problematic declustering procedures, an independent estimation of r is not available. Thus we use all three values as free model parameters. To find the best model parameters, we use the maximum likelihood approach to optimize the model fit for the considered time period $[t_s, t_e]$. For the N events occurred in this time period at times t_i $(i = 1, \ldots, N)$, the log-likelihood value as a function of the parameters $A\sigma$, $\dot{S}$ and r is given by

$$\ln L(A\sigma, \dot{S}, r) = \sum_{i=1}^{N} \ln R(t_i) - \int_{t_s}^{t_e} R(t)\mathrm{d}t = N \ln(r) - \sum_{i=1}^{N} \ln(\gamma_i \dot{S}) - r \int_{t_s}^{t_e} [\gamma(t)\dot{S}]^{-1}\mathrm{d}t \quad (11)$$

(Daley & Vere-Jones 2003). Using a grid-search for $A\sigma$ and $\dot{S}$, the corresponding value of r which maximizes the $\ln L$-value can be analytically determined in each case by

$$r = N \Big/ \int_{t_s}^{t_e} [\gamma(t)\dot{S}]^{-1}\mathrm{d}t\ . \quad (12)$$

In sum, we analyse the following set of models.

RA: Only rainfall-induced stress changes are considered, $\triangle S = \triangle S_{RA}$.

R3D: Only reservoir-induced stress changes are considered with 3-D pore-pressure diffusion, $\triangle S = \triangle S_{R3D}$.

R1D: Only reservoir-induced stress changes are considered with 1-D pore-pressure diffusion, $\triangle S = \triangle S_{R1D}$.

RA+R3D and *RA+R1D:* Rainfall- and reservoir-induced stress changes are considered simultaneously, $\triangle S = \triangle S_{RA} + \triangle S_{R1/3D}$.

All models accounting for rainfall-induced stress are calculated for the two alternative groundwater models T0d and T50d (see Section 3). For each analysed model, we determine parameters that optimize the log-likelihood value (eq. 11) for the observed earthquake activity. For the optimized models, we also calculate the linear correlation coefficient C (cross-correlation with zero delay) between the forecasted and earthquake rates.

5 RESULTS

The resulting parameters of the maximum likelihood fit are listed in Table 2 for the different models, together with the resulting correlation coefficients (C) and the value of the AIC, where the best model is indicated by the minimum AIC-value. The AIC-value is defined as $2(n - \ln L)$ with n being the number of free model parameters and $\ln L$ being the log-likelihood value defined in eq. (11). Note that $\exp(-\Delta\mathrm{AIC}/2)$ can be interpreted as the relative probability that the corresponding model (and not the model with minimum AIC-value) minimizes the (estimated) information loss (Burnham & Anderson 2002).

The corresponding time-dependent model forecasts are shown in Fig. 6 in comparison to the observation, and the cross-correlations are presented in Fig. 7 as a function of the delay between the model forecast and the seismicity. The correlation coefficients between model rates and seismicity are significantly higher than the

Table 2. Optimized model parameters where the best-fitting result is highlighted in bold.

Model[a]	Model parameter				Fit quality	
	D (m^2 s^{-1})	$A\sigma$ (Pa)	$\dot{S}$ (Pa yr^{-1})	r (yr^{-1})	AIC–AIC$_{\min}$[b]	C[c]
RA(T0d)	5	985	52	79	125	0.38
RA(T50d)	100	859	21	41	67	0.59
R3D	50	9	0.3	43	**0**	0.72
R1D	100	6755	1470	85	37	0.72
RA(T0d)+R3D	5	964	44	70	119	0.39
RA(T50d)+R3D	100	871	19	37	62	0.59
RA(T0D)+R1D	100	6916	1236	76	26	0.76
RA(T50d)+R1D	100	6901	1636	85	21	**0.77**

[a]T0d refers to RA-models based on the groundwater model with immediate recharge, while T50d refers to the corresponding results for the groundwater model with delayed recharge.
[b]Akaike information criterion AIC $= 2(n - \ln L)$ with n and $\ln L$ being the number of free model parameters and the log-likelihood value (eq. 11), respectively.
[c]C = correlation coefficient calculated for Gaussian smoothed earthquakes with standard deviation of 30 d.

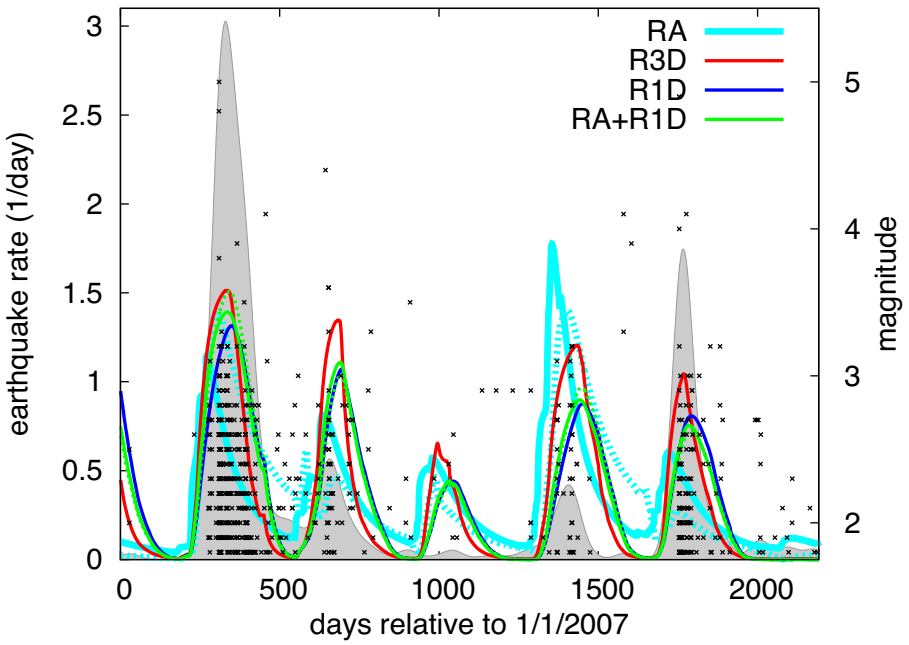

Figure 6. The forecasted number of events per day (curves) in comparison to the observed earthquakes (dots) and rates (grey shaded). The corresponding model parameters are given in Table 2. RA-models represented by solid lines are based on the groundwater model with immediate recharge (T0d), while the dashed lines refer to the corresponding results for the groundwater model with delayed recharge (T50d). Note that the result of model RA+R3D is not shown because it is almost identical to the result of model RA.

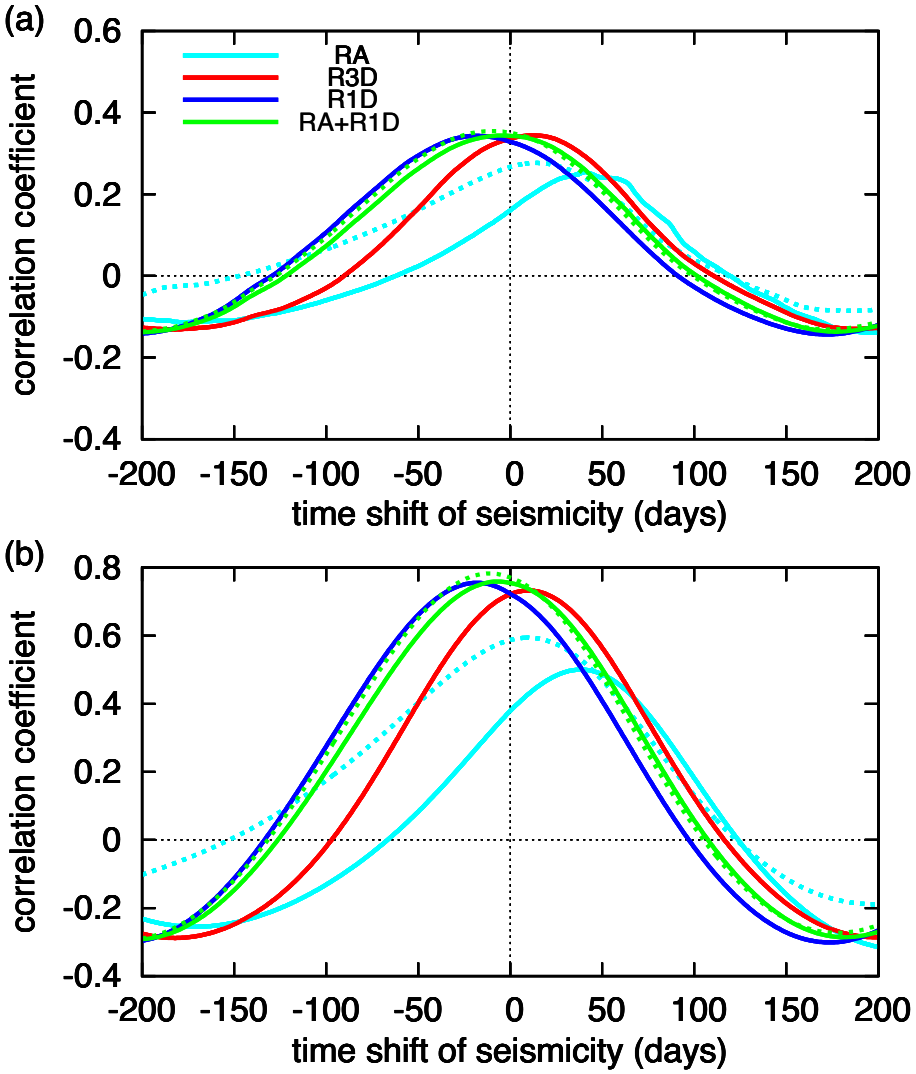

Figure 7. Cross-correlation coefficients between models and seismicity, done in exactly the same way as in Fig. 4 for the observables. RA-models represented by solid lines are based on the groundwater model with immediate recharge (T0d), while the dashed lines refer to RA-models based on the groundwater model with delayed recharge (T50d). Note that the result of model RA+R3D is not shown because it is almost identical to the result of model RA.

correlations between the hydrological observables and seismicity shown in Fig. 4. Furthermore, no significant delay for the models based on reservoir-induced stresses are now found. For all models, the probability is less than 0.1 per cent that the observed correlation values (without time-shift) could be observed by chance in the case that model results and observations are uncorrelated.

Although none of our simple models can perfectly match the absolute size of the observed seismic response in the different time periods, Fig. 6 shows that the models are able to forecast not only the timing of the four main seismicity swarms in the analysed time period, but also generally their relative strength. The first year swarm is predicted to be the strongest in agreement with the observations. Also the decaying amplitudes in the following two years is correctly reproduced, as well as the intermediate level of activity in the fourth year. Only the relative strong swarm activity in the fifth year is underestimated in the models.

A simple visual comparison with pore-pressure curves (see Fig. 5) could not explain the observed relative difference of the strength of the seismic response to the different loading cycles. Thus the ability to approximately reproduce the relative strength of the observed seismic swarm phases demonstrates the importance of quantitative seismicity models which account for the absolute stress changes and rate- and state-dependent frictional earthquake nucleation.

The best model in terms of the highest likelihood value is the reservoir model R3D with 3-D pore pressure diffusion, but it results in a completely unrealistic value of $A\sigma = 9$ Pa. However, significantly higher and more realistic estimates of $A\sigma$-values are obtained if 1-D instead of 3-D pore-pressure diffusion related to the reservoirs is assumed. In this case, the resulting values of $A\sigma$ are approximately 7 kPa, which is only a bit smaller than the values typically found for seismicity in active tectonic areas which are in the range between 10 and 200 kPa (Hainzl *et al.* 2010). Furthermore, not only the parameters are more reasonable but also the fit in terms of correlation coefficients is superior. The 1-D reservoir model in combination with rainfall induced pressure changes results in the highest correlation coefficient of 0.77 (see Table 2).

Ignoring reservoir-induced pressure changes leads to worsen fits of the data. The pure rainfall model fits worse than the other models. Also the combination with reservoir-induced 3-D pore pressure diffusion (model RA+R3D) cannot improve the fit significantly,

because the calculated pressure changes of the R3D model are much smaller than the estimated rainfall-induced pressure changes in the analysed seismogenic volume. Thus the overall stress history in the combined model RA+R3D is dominated by the rainfall-related stress changes leading to a very similar result as the pure rainfall model (RA).

6 DISCUSSION

Our model approach remains simplistic due to the lack of information about the crustal structure and detailed surface conditions. Thus our estimations of time-dependent pore-pressure changes at depth can be seen only as a first-order approximation. However, they can be used to compare the relative importance of alternative hypothesis. For example, our analysis clearly shows that the reservoirs cannot explain the seismicity if the crust is homogeneous. In this case, the 3-D pore-pressure diffusion in addition to the static load would only create tiny stress changes in the seismically active region. To explain the observed seismicity in this case, a tiny friction resistance $A\sigma = 9$ Pa has to be assumed, which is unrealistic, because tidal stresses would be then expected to dominate the activity (Hainzl *et al.* 2013b). However, our results indicate that channels of high permeability are likely existing, where pressure changes can be approximated by 1-D pore-pressure diffusion. The existence of such fracture zones connecting the reservoir with the approximately 10–20 km distant seismically active region would explain much higher induced stresses leading to an estimated value of $A\sigma = 7$ kPa which is comparable to estimates in tectonic regions. Thus the crust in the Talala region does not need necessarily to be in a highly critical state to explain the seismicity. Anyway, reservoir and rainfall triggering is expected to act simultaneously. Thus further credibility of our modelling results comes from the fact that accounting simultaneously for both mechanisms, 1-D reservoir effects and rainfall-induced stress changes resulting from areal water infiltration in the ground, leads to the highest correlation coefficients. Thus our results are physically reasonable.

Our estimations of the hydraulic diffusivity seems to be in an apparent contradiction. While our graphical approach in Fig. 5 leads to an estimation of approximately 5 $m^2\ s^{-1}$, the log-likelihood estimations of the seismicity model yields an estimation of 50–100 $m^2\ s^{-1}$. This might have several reasons. One reason is that the rate- and state-dependent frictional nucleation of earthquakes leads to a delayed response of the activity to stress changes. In particular, a single stress step will lead to a Omori-type decay of delayed triggered seismicity in a time period of $A\sigma/\dot{S}$. Thus delayed seismicity can occur after the pore-pressure increase, while our simple graphical approach assumes instantaneous triggering. Furthermore, the full spatiotemporal stress history is taken into account in the seismicity model, while the reservoirs cycles are approximated by boxcar functions and treated spatially and temporally as independent in the graphical approach. Thus the estimation based on the seismicity model should be superior. Anyway, the value of the hydraulic diffusivity is not well constrained by the spatially clustered data and our results only indicate that the hydraulic diffusivity has to be rather large to explain the data.

7 CONCLUSION

We have tested the hypothesis of rainfall- and reservoir-triggering in the region of Talala, Gujarat, India. For that purpose, we calculate the seismicity response based on rate- and state-dependent frictional earthquake nucleation resulting from time-dependent stress changes which are induced by areal water infiltration due to rainfall and localized loading and infiltration due to reservoir level variations in addition to constant tectonic stressing. Our approach allows in general a quantitative comparison with observed time-dependent earthquake occurrences in the 3-D space. In our specific application, however, we only compare seismicity forecasts integrated over the seismogenic volume to reduce the effect of the location uncertainties. Our comprehensive analysis indicates that surface water supply seems to be the driving force for the swarm activity in this region. The model can reproduce not only the timing of the observed seismicity but also the relative strength of the activity in general. Our results show that although rainfall-triggering can partly explain the observations, reservoir triggering is an important driving force, if pore-pressure diffusion occurs in channel-like features (e.g. fracture zones) connecting the reservoirs to the active fault zone. The highest correlations are observed for the physically reasonable case that stress changes related to both rainfall and reservoirs sum up, supporting our hypothesis of hydraulic triggered seismicity in Talala, Gujarat, region.

ACKNOWLEDGEMENTS

Thanks to DST, Gujarat and DST, New Delhi, for providing all necessary support. We are also grateful to the two anonymous reviewers for their helpful comments and the chief executive engineer of Narmada, Water Resources, Water Supply and Kalpsar Department for providing the data of Hiran I and II reservoir.

REFERENCES

Biswas, S.K., 1987. Regional framework, structure and evolution of the western marginal basins of India, *Tectonophysics,* **135,** 302–327.

Burnham, K.P. & Anderson, D.R., 2002. *Model Selection and Multimodel Inference: A Practical Information-Theoretic Approach,* Springer-Verlag, paragraph 6.4.5.

Catalli, F., Cocco, M., Console, R. & Chiaraluce, L., 2008. Modeling seismicity rate changes during the 1997 Umbria-Marche sequence (Central Italy) through a rate and state-dependent model, *J. geophys. Res.,* **113,** B11301, doi:10.1029/2007JB005356.

Cocco, M. & Rice, J.R., 2002. Pore pressure and poroelasticity effects in Coulomb stress analysis of earthquake interactions, *J. geophys. Res.,* **107,** B2, ESE 2-1–ESE 2-17.

Costain, J.K. & Bollinger, G.A., 2010. Review: research results in hydroseismicity from 1987 to 2009, *Bull. seism. Soc. Am.,* **100,** 1841–1858.

Daley, D.J. & Vere-Jones, D., 2003. *An Introduction to the Theory of Point Processes I,* Springer.

Deng, K., Zhou, S., Wang, R., Robinson, R., Zhao, C. & Cheng, W., 2010. Evidence that the 2008 Mw 7.9 Wenchuan earthquake could not have been induced by the Zipingpu Reservoir, *Bull. seism. Soc. Am.,* **100,** 2805–2814.

Dieterich, J.H., 1994. A constitutive law for rate of earthquake production and its application to earthquake clustering, *J. geophys. Res.,* **99,** 2601–2618.

Dieterich, J.H., Cayol, V. & Okubo, P., 2000. The use of earthquake rate changes as a stress meter at Kilauea volcano, *Nature,* **408,** 457.

Enescu, B., Hainzl, S. & Ben-Zion, Y., 2009. Correlations of seismicity patterns in Southern California with surface heat flow data, *Bull. seism. Soc. Am.,* **99,** 3114–3123.

Evangelides, C., Arampatzis, G. & Tzimopoulos, C., 2010. Estimation of soil moisture profile and diffusivity using simple laboratory procedures, *Soil Sci.,* **175,** 118–127.

Fischer, T., Hainzl, S., Eisner, L., Shapiro, S.A. & Le Calvez, J., 2008. Microseismic signatures of hydraulic fracture growth in sediment formations: observations and modeling, *J. geophys. Res.,* **113,** B02307, doi:10.1029/2007JB005070.

Gahalaut, K. & Hassoup, A., 2012. Role of fluids in the earthquake occurrence around Aswan reservoir, Egypt, *J. geophys. Res.,* **117,** B02303, doi:10.1029/2011JB008796.

Gandhi, D., Prajapati, P., Prizomwala, S.P., Bhatt, N. & Rastogi, B.K., 2014. Delineating the spatial variability in neotectonic activity along southwestern Saurashtra, Western India, *Zeitschrift f. Geomorphologie,* doi:10.1127/0372-8854/2014/0122.

Hainzl, S., Kraft, T., Wassermann, J. & Igel, H., 2006. Evidence for rain-triggered earthquake activity, *Geophys. Res. Lett.,* **33,** L19303, doi:10.1029/2006GL027642.

Hainzl, S., Enescu, B., Cocco, M., Woessner, J., Catalli, F., Wang, R. & Roth, F., 2009. Aftershock modeling based on uncertain stress calculations, *J. geophys. Res.,* **114,** B05309, doi:10.1029/2008JB006011.

Hainzl, S., Steacy, S. & Marsan, D., 2010. Seismicity models based on Coulomb stress calculations, Community Online Resource for Statistical Seismicity Analysis, doi:10.5078/corssa-32035809. Available at: http://www.corssa.org, last accessed 1 August 2014.

Hainzl, S., Zakharova, O. & Marsan, D., 2013a. Impact of aseismic transients on the estimation of aftershock productivity parameters, *Bull. seism. Soc. Am.,* **103,** 1723–1732.

Hainzl, S., Ben-Zion, Y., Cattania, C. & Wassermann, J., 2013b. Testing atmospheric and tidal earthquake triggering at Mt. Hochstaufen, Germany, *J. geophys. Res.,* **118,** 5442–5452.

King, G.C.P. & Cocco, M., 2001. Fault interaction by elastic stress changes: New clues from earthquake sequences, *Adv. Geophys.,* **44,** 1–38.

Marsan, D., Prono, E. & Helmstetter, A., 2013. Monitoring aseismic forcing in fault zones using earthquake time series, *Bull. seism. Soc. Am.,* **103,** 169–179.

Mavko, G., Mukerji, T. & Dvorkin, J., 2009. *The Rock Physics Handbook: Tools for Seismic Analysis of Porous Media,* 2nd edn, Cambridge Univ. Press.

Miller, S.A, 2008. Note on rain-triggered earthquakes and their dependence on karst geology, *Geophys. J. Int.,* **173,** 334–338.

Muco, B., 1995. The seasonality of Albanian earthquakes and crosscorrelation with rainfall, *Phys. Earth planet. Int.,* **88,** 285–291.

Niu, G.-Y., Yang, Z.-L., Dickinson, R.E., Gulden, L.E. & Su, H., 2007. Development of a simple groundwater model for use in climate models and evaluation with Gravity Recovery and Climate Experiment data, *J. geophys. Res.,* **112,** D07103, doi:10.1029/2006JD007522.

Ogata, Y., 1988. Statistical models for earthquake occurrence and residual analysis for point processes, *J. Am. Stat. Assoc.,* **83,** 9–27.

Parotidis, M., Shapiro, S.A. & Rothert, E., 2004. Back front of seismicity induced after termination of borehole fluid injection, *Geophys. Res. Lett.,* **31,** L02612, doi:10.1029/2003GL018987.

Rastogi, B.K., Kumar, S., Aggarwal, S.K., Mohan, K., Rao, N., Rao, P.C. & Kothyari, G.C., 2012a. The October 20, 2011 Mw 5.1 Talala earthquake in the stable continental region of India, *Nat. Hazards,* **65**(2), 1197–1216.

Rastogi, B.K., Kumar, S. & Aggarwal, S.K., 2012b. Seismicity of Gujarat, *Nat. Hazards,* **65,** 1027–1044.

Roeloffs, E.A., 1988. Fault stability changes induced beneath a reservoir with cyclic variations in water level, *J. geophys. Res.,* **93,** 2107–2124.

Shapiro, S.A., Huenges, E. & Borm, G., 1997. Estimating the crust permeability from fluid-injection-induced seismic emission at the KTB site, *Geophys. J. Int.,* **131,** F15–F18.

Shapiro, S.A., Patzig, R., Rothert, E. & Rindschwentner, J., 2003. Triggering of seismicity by pore-pressure perturbations: permeability-related signatures of the phenomenon, *Pure appl. Geophys.,* **160,** 1051–1066.

Simpson, G., 2001. Influence of compression-induced fluid pressures on rock strength in the brittle crust, *J. geophys. Res.,* **106,** 19 465–19 478.

Svejdar, V., Küchenhoff, H., Fahrmeir, L. & Wassermann, J., 2011. External forcing of earthquake swarms at Alpine regions: example from a seismic meteorological network at Mt. Hochstaufen SE-Bavaria, *Non. Proc. Geophys.,* **18,** 849–860.

Talwani, P., 1997. On the nature of reservoir-induced seismicity, *Pure appl. Geophys.,* **150,** 473–492.

Utsu, T., Ogata, Y. & Matsu'ura, R.S., 1995. The centenary of the Omori formula for a decay of aftershock activity, *J. Phys. Earth,* **43,** 1–33.

Zoback, M.D. & Harjes, H.-P., 1997. Injection-induced earthquakes and crustal stress at 9 km depth at the KTB deep drilling site, Germany, *J. geophys. Res.,* **102,** 18 477–18 492.